THE JOURNAL OF PHYSICAL CHEMISTRY C

Article

Cite This: J. Phys. Chem. C 2019, 123, 1160−1169

pubs.acs.org/JPCC

First-Principles Kinetic Study for Ostwald Ripening of Late Transition Metals on TiO_2(110)

Qixin Wan,[†,∥,⊥] Sulei Hu,[‡,§,⊥] Jiangnan Dai,[†] Changqing Chen,[*,†] and Wei-Xue Li[*,‡,§]

[†]Wuhan National Laboratory for Optoelectronics, Huazhong University of Science and Technology, Wuhan 430074, China

[‡]Department of Chemical Physics, School of Chemistry and Materials Science, iChEM, CAS Center for Excellence in Nanoscience, University of Science and Technology of China, Hefei 230026, China

[§]Hefei National Laboratory for Physical Sciences at the Microscale, Hefei 230026, China

[∥]Key Laboratory for Optoelectronics and Communication of Jiangxi Province, Jiangxi Science and Technology Normal University, Nanchang 330013, China

Supporting Information

ABSTRACT: Supported transition metal (TM) particles on oxides severely deactivate because of sintering. Investigation of the dependence of Ostwald ripening kinetics on the composition and size of the metal particles is essential for understanding the sintering mechanism. On the basis of the first-principles kinetics simulation, we study here the ripening kinetics of TiO_2(110)-supported late TMs (including Ni, Cu, Ru, Rh, Pd, Ag, Ir, Pt, and Au) in a wide range of particle size. Density functional theory calculations show that the total activation energies of ripening are decided by the corresponding formation energy of the metal monomer on TiO_2(110) and vary in the range of 3 eV following the order of Ag < Cu < Pd < Au < Ni < Rh < Pt < Ru < Ir. Isothermal and temperature ramping kinetic simulations are performed, and the corresponding half-life time and onset temperature of ripening are extracted, respectively. The results show that the half-life time of ripening exponentially increases with the total activation energy of the metal from Ag to Ir. The onset temperature of ripening increases more than hundreds of kelvin, which is consistent with variation in the melting points of the bulk counterpart. The ripening rate is found to dramatically increase with the decrease of the particle size, and the corresponding size effect increases pronouncedly with the total activation energy from Ag to Ir. This work provides valuable insights into the ripening kinetics of oxide-supported metal particles and is helpful in designing stable nanocatalysts.

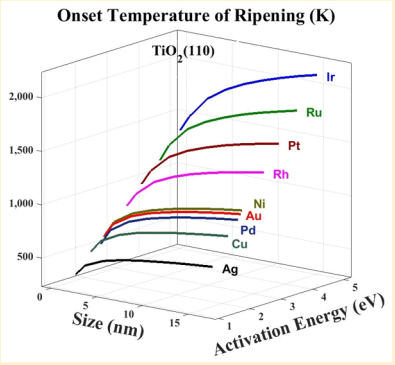

1. INTRODUCTION

Transition metals (TMs) have attracted great attention for their broad range of applications in surface science,[1] heterogeneous catalysis,[2] electronic devices,[3] gas sensors,[4] and so forth. To increase atom utilization and save the cost, in particular for precious group metals, TMs are often prepared in small sizes.[5] Though small particles may expose more active low-coordination sites and show unique quantum size effects, the high specific surface energy destabilizes corresponding particles, which tend to sinter and grow to larger ones with a lower surface area.[6−8] Sintering may proceed via Ostwald ripening (OR),[9−11] in which large particles grow at the expense of smaller ones through the migration of atoms or particle migration and coalescence (PMC)[12−14] in which metal particles diffuse and coalesce with neighboring particles as a whole. Sintering kinetics depend sensitively on support surface orientation[15,16] and thereupon defects[17] and preadsorbed species,[18] reaction atmosphere,[19] metal composition,[20] particle morphology,[21] size[22,23] and spatial distribution,[24] and so forth. Investigation of sintering kinetics, in particular, thermal stability and long-time durability, is vital for the rational design of practical catalysts but remains a challenge.

Various oxides have been used as supports to disperse and stabilize metal particles. Among others, titanium dioxide has been widely used because of its strong interfacial interaction with TMs and excellent stability under ambient conditions.[25] Especially, the sintering behavior of the late TMs including 3d (Ni[26,27] and Cu[28,29]), 4d (Ru,[30,31] Rh,[32,33] Pd,[34,35] and Ag[36,37]), and 5d (Ir,[38,39] Pt,[40,41] and Au[42,43]) elements supported on TiO_2(110) were frequently observed in experiments. Typically, sintering of Au particles on TiO_2(110) during CO oxidation was believed to be dominated by the OR mechanism.[44] Scanning tunnel microscopy (STM) monitoring of Pt particles on rutile TiO_2(110) and subsequent kinetic simulations suggested that the PMC mechanism is responsible for the observed sintering process.[45] The sintering behavior of relatively small Pd particles (less than 1 nm) on TiO_2(110)

Received: August 31, 2018
Revised: December 17, 2018
Published: December 19, 2018

DOI: 10.1021/acs.jpcc.8b08530
J. Phys. Chem. C 2019, 123, 1160−1169

was also found to be dominated by the PMC mechanism because of the observed lognormal-like particle size distribution (PSD) attributed to the PMC mechanism with a tail toward the direction of larger size,[46] whereas for a relatively large particle size,[47] the evolution of PSD observed by real-time STM indicated that the OR mechanism dominated the sintering process. Thus, the sintering mechanism is not only composition-dependent but also particle size-dependent. Moreover, the particle size also affects the sintering rate, as explored early by Wynblatt and Gjostein.[48] Size effect on the sintering of TiO_2(110)-supported Au was studied based on the OR mechanism.[49] Quantitative experimental study indicated that the sintering rate of supported Pd particles with a larger initial particle size was slower than that with smaller ones.[50] Recently, we studied the influence of PSD on OR kinetics by solving the corresponding rate equation over a wide range of particle size and degree of dispersion.[51] It was found that although decreasing the particle size for higher dispersion worsens the stability severely, increasing the size monodispersity could significantly improve the stability. To the best of our knowledge, however, the influence of composition and size of the late TM particles on rutile TiO_2(110) on the OR kinetics and their characteristic onset temperature and long-time durability have not been investigated yet.

The purpose of the present work is to study the impact of the composition and initial average particle size on OR of the late TM particles on rutile TiO_2(110) using first-principles ripening kinetic simulation.[51−53] The late TMs considered include Ni, Cu, Ru, Rh, Pd, Ag, Ir, Pt, and Au. The corresponding total activation energies of ripening on rutile TiO_2(110) were calculated by density functional theory (DFT) and are discussed in detail. We analyzed the evolution of PSD, dispersion, average particle size, and total particle number of TiO_2(110)-supported Au particles under temperature-programmed aging (TPA) and isothermal condition, from which the corresponding long-time durability and thermal stability of ripening were derived. Influence of composition on the onset temperature and half-life time of ripening was examined systematically and compared with the available experimental results. Moreover, the ripening kinetics of supported late TMs have been investigated in a wide range of initial average size, and the corresponding kinetic behaviors and dependence on composition have been analyzed. An empirical formula between the onset temperature of ripening and the melting temperature of the bulk metal mediated by the particle size was also proposed.

2. THEORETICAL METHODS

2.1. Ripening Kinetics. For OR of supported particles,[49,54] the atom detaches first from the small particle edge and lands in the interfacial region between the particle and the support (Figure 1). Subsequently, the atoms leave the interfacial region and diffuse on the support to approach the large particles in the neighborhood. Under the steady state, the atoms detaching from the particle edge are equal to the atoms leaving the interfacial region. Namely, the net flux of the atoms in the interfacial region is zero. The resulting ripening rate equation for a particle with a given curvature radius of R is

$$\frac{dR}{dt} = A(R)\left(\exp\left[\frac{\Delta\mu(R^*)}{k_BT}\right] - \exp\left[\frac{\Delta\mu(R)}{k_BT}\right]\right)\exp\left[-\frac{E_{tot}}{k_BT}\right] \quad (1)$$

The equation consists mainly of three key parts, prefactor $A(R)$, chemical potential $\Delta\mu(R)$, and total activation energy E_{tot}. Prefactor $A(R)$ depends sensitively on the ripening mechanism (interface or diffusion control), geometrical factor, and size of supported particles

$$A(R) = \frac{XY}{X+Y}\frac{K}{R^2} \quad (2)$$

where $X = 2\pi a_0 R\sin(\alpha)$, $Y = 2\pi a_0^2/\ln[L/R\sin(\alpha)]$, and $K = \nu_s\Omega/[4\pi a_0^2\alpha_1]$. α is the contact angle between the metal particle and the support and depends sensitively on the particle composition, size, metal particle−support interaction, and reaction conditions.[55,56] a_0 is the lattice constant of the support surface, L is the diffusion length of the monomer, ν_s is the vibrational frequency of the monomer on the support surface (6×10^{13} s^{-1} was used in present work), Ω is the molar volume of the bulk metal atom, $\alpha_1 = (2 - 3\cos\alpha + \cos^3\alpha)/4$ is the geometrical factor, k_B is the Boltzmann constant, and T is the temperature.

Chemical potential of the atoms in supported particles with spherical shape $\Delta\mu(R)$ is approximated here by the Gibbs−Thomson (G−T) relation with energy reference of the bulk counterpart[57]

$$\Delta\mu(R) = \frac{2\Omega\gamma}{R} \quad (3)$$

γ is the surface energy of the supported metal particles, which could be morphology-dependent,[58] function of the particle size,[59] and sensitive to the metal−support interaction[60−62] and adsorption of reactants.[63] The facet-dependent surface energy, taking Rh[64] as an example, was reported in our previous work.[54] The G−T-like relation explicitly taking into account the effect of supports was addressed recently.[61]

R^* is the critical radius with which the corresponding particle will neither grow nor shrink. To account properly for the mass balance during OR, R^* should be calculated accurately. For diffusion control and interface control limit, R^* can be calculated directly as reported in ref 9. Otherwise, R^* has to be solved numerically, and the details can be found in our recent work.[53] Initial PSD was assumed to follow a Gaussian distribution $f(R,t)$ with an average curvature radius $\langle R\rangle$ and a relative standard deviation (rsd). In practice, the projection diameter $\langle d\rangle$ of the spherical particle on the support rather than the curvature of radius is used, and $\langle d\rangle = 2\langle R\rangle$ for $\alpha = 90°$. During OR, the total mass and volume are conserved, namely, $4\pi\alpha_1/3\int_0^\infty f(R,t)R^3\,dR = V_0$ (V_0 is the initial total volume of supported metal particles). From the evolution of $f(R,t)$, the total particle number $N(t) = \int_0^\infty f(R,t)dR$, dispersion, surface area, average size, and so forth could be extracted.[51,53] Further, the ripening kinetic simulations under both isothermal and temperature ramping conditions are performed. The characteristic half-life time and onset temperature of ripening are quantified.

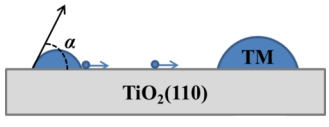

Figure 1. Schematic representation of supported TM particles with contact angle α and atoms emitting from the particle, following migrating to the interface and further diffusing on TiO_2(110).

DOI: 10.1021/acs.jpcc.8b08530
J. Phys. Chem. C 2019, 123, 1160−1169

Recently, we studied in detail the influence of the surface energy, the contact angle, and the total activation energy on sintering kinetics.[53] It was found that varying the surface energy in magnitude of 30 meV/Å^2 (typical difference in the surface energy between open and close-packed facets) only changes the lifetime of ripening by a factor of 3, and varying the contact angle of 30° changes the lifetime by a factor of 6. Whereas the total activation energy of the TM studied in the present submission varied in the range of 3 eV (see below), this will change the lifetime by more than 15 orders of magnitude. In other words, for the trend study of the late TM ripening on supports, using the bulk surface energy[65] (149 meV/Å^2 for Ni, 112 meV/Å^2 for Cu, 190 meV/Å^2 for Ru, 166 meV/Å^2 for Rh, 125 meV/Å^2 for Pd, 77 meV/Å^2 for Ag, 190 meV/Å^2 for Ir, 155 meV/Å^2 for Pt, and 94 meV/Å^2 for Au) and a fixed contact angle of 90° would be a good approximation and are used throughout the present work.

2.2. DFT Calculations. DFT calculations were performed using the Vienna Ab initio Simulation Program[66−68] based on the projector-augmented wave method. We used the revised Perdew−Burke−Ernzerhof (RPBE) exchange−correlation functional, which is believed to better describe the surface adsorption, alleviating the potential over binding.[69] The kinetic energy cutoff for the plane wave basis set is 400 eV, and the spin polarization was considered as well. The optimized crystal parameters of rutile TiO_2 bulk are a = 4.661 Å and c = 2.968 Å, which are comparable with the experimental values of a = 4.593 Å and c = 2.958 Å.[70] A (2 × 4) surface supercell of rutile TiO_2(110) with a slab of four Ti−O layers that was separated from its periodic images by a vacuum space of 15 Å was used. The Γ point was used to sample the surface Brillouin zone, as has been done in previous studies involving TiO_2.[71] For the late TM adsorption on the surface considered [corresponding 1/8 monolayer (ML)], the top two Ti−O layers and the adsorbates were allowed to relax while the other atoms in the bottom layers were fixed in their bulk truncated positions. Optimization was carried out by using the conjugate-gradient algorithm until the Hellman−Feynman force[72] on each atom was less than 0.03 eV/Å.

Total activation energy E_{tot} for OR of supported metal particles is the sum of the formation energy E_f of the metal monomer on supports (with respect to the bulk metal counterpart) and the diffusion barrier E_d of the metal monomer on supports, namely, $E_{tot} = E_f + E_d$. E_f was computed by

$$E_f = E_{ma/ox} - E_{ox} - E_B \quad (4)$$

where $E_{ma/ox}$, E_{ox}, and E_B are the total energy of the metal atom on support, the support, and the bulk metal atom, from DFT. To calculate the diffusion barrier E_d, climbing image nudged elastic band (CI-NEB) method[73,74] was utilized to locate the transition states (TSs) for the diffusion of the TM adatom on the support surface. At least seven images (including the initial and final states) were used, and the TSs optimized were confirmed by vibrational analysis showing a single imaginary mode. Zero-point energies and entropy corrections were neglected in the present work.

3. RESULTS AND DISCUSSION

3.1. DFT Calculations. We first describe the calculated formation energy E_f of the late TM atoms (Ag, Cu, Au, Pd, Ni, Rh, Pt, Ru, and Ir) on TiO_2(110). Various adsorption sites (Figure 2) were considered, and only the most stable configurations optimized are shown in Figure 3. It is found that the preferential adsorption site is composition-dependent.

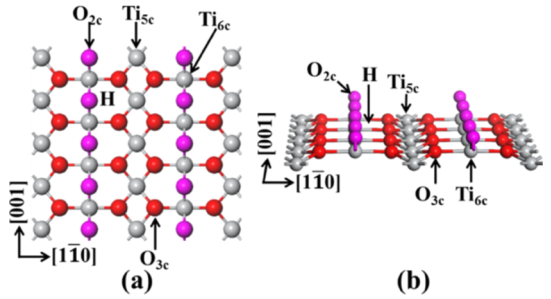

Figure 2. Top (a) and side (b) views of the topmost TiO_2(110) surface. Gray balls represent titanium atoms, and magenta and red balls represent upmost bridge and in-plane oxygen, respectively.

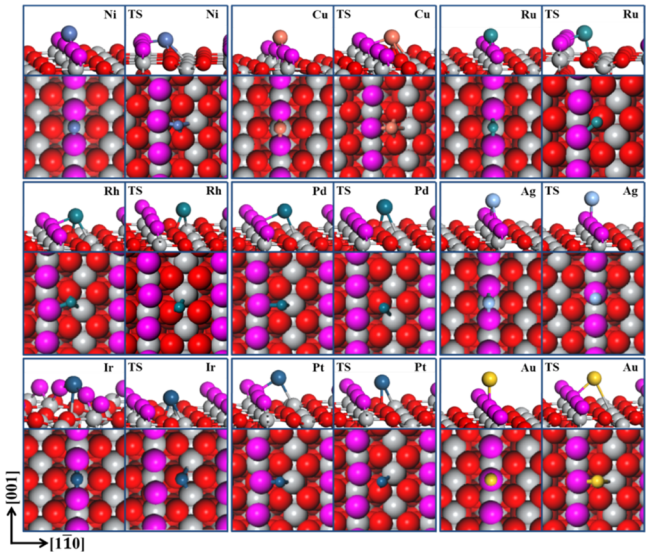

Figure 3. Side view (top) and top view (bottom) for the most stable site (IS) and corresponding TS of late TMs on TiO_2(110). Gray balls represent titanium atoms, magenta and red balls represent the upmost bridging oxygens and lattice oxygens, respectively.

Ni, Cu, Ru, Ag, and Ir prefer the bridge site of two protruded two-coordinated oxygen (O_{2c}). Pd and Pt prefer the bridge site of O_{2c} and in-plane fivefold coordinated Ti (Ti_{5c}), and Rh is similar but tilted slightly toward one in-plane three-coordinated oxygen (O_{3c}), whereas Au prefers the top site of O_{2c}. The site preferences are in good agreement with the previous calculations of Cu, Ag, Au and Ni,[75] Pd,[76,77] Pt[78,79] and Rh.[80]

Calculated formation energies of TM atoms on TiO_2(110) are plotted in Figure 4 and Table 1. All these formation energies are considerably endothermic (1.25 eV at least), meaning that the equilibrium concentration of TM adatoms being responsible for OR is rather low. The lowest and highest E_f calculated are Ag and Ir with a value of 1.25 and 4.11 eV, respectively. Results for remaining TMs follow the order of Ag (1.25 eV) < Cu (1.35 eV) < Ni (1.74 eV) < Pd (2.05 eV) < Au (2.23 eV) < Rh (2.86 eV) < Pt (3.11 eV) < Ru (3.74 eV) < Ir (4.11 eV). We note that the calculated formation energies vary significantly in magnitude of about 3 eV, indicating that even for the late TMs considered here, ripening kinetics between different TMs considered will be very different, as seen clearly

DOI: 10.1021/acs.jpcc.8b08530
J. Phys. Chem. C 2019, 123, 1160−1169

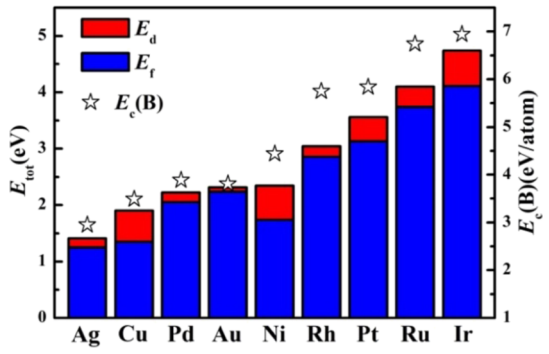

Figure 4. Calculated total activation energy (E_{tot}), summation of diffusion barrier (E_d), and formation energy (E_f) of late TMs on TiO_2(110) as well as the corresponding cohesive energy E_c(B) of bulk metals from ref 81.

Table 1. Calculated Formation Energy E_f, Diffusion Barrier E_d, and Total Activation Energy E_{tot} of Late TMs on Rutile TiO_2(110) and Melting Temperatures of Bulk Metal[81]

metal	E_f/eV	E_d/eV	E_{tot}/eV	T_m(B)/K
Ni	1.74	0.60	2.34	1728
Cu	1.35	0.55	1.90	1358
Ru	3.74	0.36	4.10	2527
Rh	2.86	0.18	3.04	2236
Pd	2.05	0.17	2.22	1827
Ag	1.25	0.16	1.41	1235
Ir	4.11	0.63	4.74	2720
Pt	3.11	0.40	3.51	2045
Au	2.23	0.08	2.31	1338

below. We note that when the PBE functional was used, the calculated formation energies are about 0.03−0.29 eV greater (Table S2). Compared to the alteration of the formation energy on different TMs considered in magnitude of about 3 eV, the effect of different exchange−correlation functionals is small and will not influence the conclusion of the present work.

Diffusion of metal atoms along both [001] and [1$\bar{1}$0] directions was investigated to find the favorable diffusion pathway (Table S1). The optimized TSs with a lower diffusion barrier are plotted in Figure 3, and the corresponding barriers are shown in Figure 4. Though the initial states (ISs) for Ni, Cu, Ru, Ag, and Ir are the same, corresponding TSs are slightly different: both Ni and Cu are located at the bridge site of O_{2c} and Ti_{5c}, Ru at the hollow site of two O_{2c} and one O_{3c}, Ag at the top of O_{2c}, and Ir at the hollow site of two Ti_{5c} and one O_{3c}. Calculated diffusion barriers are 0.16 eV (Ag), 0.36 eV (Ru), 0.55 eV (Cu), 0.60 eV (Ni), and 0.63 eV (Ir). The difference could be attributed to their different composition and TSs. For Rh, Pd, and Pt, all optimized TSs are similar, metal atoms are located at the hollow sites of two Ti_{5c} and one O_{3c}, and the corresponding barriers are 0.18, 0.17, and 0.40 eV. TS of Au is located at the bridge site of Ti_{5c} and one O_{3c}, and the calculated barrier is only 0.08 eV. Compared to previous calculations,[75] the barriers calculated in the present work are relative smaller. This is because CI-NEB was used to identify TSs in the present work, whereas in previous literature, the potential energy surfaces were explored using an 8 × 15 uniform grid over the supercell constructed, and only the relaxation perpendicular to the surface was allowed to relax, a fact that might overestimate the corresponding barrier. Nevertheless, the calculated barriers in both works are modest and vary from 0.08 to 0.63 eV, indicating that the corresponding process is facile.

Total activation energy E_{tot}, summation of the formation energy and diffusion barrier, was derived and plotted in Figure 4 (Table 1). It can be found that E_{tot} increases in the order of Ag (1.41 eV) < Cu (1.90 eV) < Pd (2.22 eV) < Au (2.31 eV) < Ni (2.34 eV) < Rh (3.04 eV) < Pt (3.51 eV) < Ru (4.10 eV) < Ir (4.74 eV). The lowest one is 1.41 eV of Ag, and the highest one is 4.74 eV of Ir, with differences as large as 3.33 eV. Obviously, the difference in E_{tot} mainly comes from the formation energy rather than the diffusion barrier. This indicates that the ripening of the late TMs considered on TiO_2(110) would be interface-controlled, a fact that supports well the previous proposals found in the ripening of supported Au,[44,49] Rh,[82] Ni,[83] and Cu[83] particles. As a reference, the cohesive energies of the TMs considered are plotted in Figure 4 as well. Not unexpected, the higher the cohesive energy, the higher the formation energy and hence the total activation energy of ripening.

3.2. Composition Effect. *3.2.1. Temperature Program Aging.* On the basis of the present DFT results, we first investigated the ripening kinetics of TiO_2(110)-supported Au particles under TPA. The average size $\langle d_0 \rangle$ = 3.88 nm and rsd = 25% extracted from the experiment[84] were used as the initial Gaussian PSD for Au/TiO_2(110). Linear temperature ramping starts from 200 K at a rate of 1 K/s, if not specified otherwise, and the results are plotted in Figure 5. For temperature T

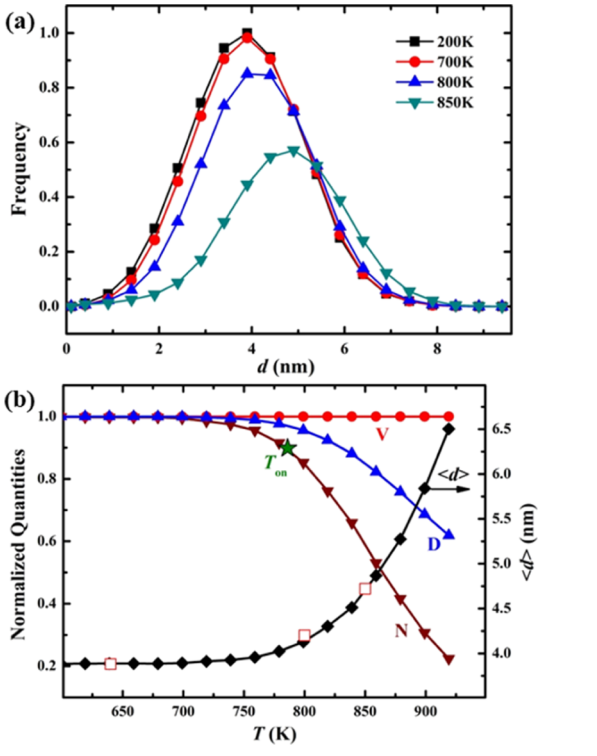

Figure 5. (a) Snapshots of PSD of Au particles on TiO_2(110) with respect to linear ramping temperature from 200 K at a rate of 1 K/s and (b) evolution of the corresponding normalized volume V (circle), dispersion D (triangle), particle number N (inverted triangle), and average diameter $\langle d \rangle$. Onset temperature T_{on} is indicated by the green star. The contact angle α = 90°, initial $\langle d_0 \rangle$ = 3.88 nm, and rsd = 25%. The diameter $\langle d \rangle$ of open squares is calculated according to the relation between the height H and diameter $\langle d \rangle$ ($\langle d \rangle$ = 2H + 2.52 nm) on the basis of the height from ref 84.

DOI: 10.1021/acs.jpcc.8b08530
J. Phys. Chem. C 2019, 123, 1160−1169

lower than 700 K, a little change in the PSD and a slight increase in the size are seen. As T rises to 800 K, the peak height decreases about 16% and the peak position right shifts about 0.30 nm. With T further up to 850 K, about 43% decrease of the peak height and about 1.0 nm right shift of the peak position are recorded. Moreover, the transformation of the PSD shape from Gaussian to Lifshitz−Slyozov−Wagner (LSW) distribution with a long tail toward the small particles is seen. This originates because one larger particle grows at the expense of a few smaller particles. Figure 5b shows the evolution of the average size, normalized dispersion, and total particle number. In line with the evolution of PSD, there is no obvious change when the temperature is lower than 700 K. The average size starts to increase rapidly only when the temperature is sufficiently high. Specifically, the average size $\langle d \rangle$ increases from initial 3.88 to 3.89 nm (700 K), 4.13 nm (800 K), and 4.70 nm (850 K). With the increase of the average size, the normalized dispersion and the total particle number start to decrease accordingly.

To compare with experiments, we note that experiments often report the PSD as a function of time on realistic conditions,[44,85,86] and theoretical investigation of the influence of reactants on ripening and also on disintegration can be found in our previous works.[52,54,87] Height evolution of TiO_2(110)-supported Au particles along with the presence of stable TiO_x islands with temperature under ultrahigh vacuum was reported.[42] By assuming $\langle d \rangle = 2H + 2.52$ nm,[84] the corresponding diameter of supported Au particles could be estimated. Specifically, the average diameter of supported Au particles increases from initial 3.88 nm at room temperature to approximately 4.20 nm (800 K) and 4.72 nm (850 K) (open squares indicated in Figure 5b), which are in good agreement with the present calculation. Interestingly, experimental data also indicates that the ripening initiates only when the temperature was sufficiently high. The threshold temperature for initiating the ripening is defined therefore as the onset temperature, T_{on}, at which the particle number has decreased to 90% of the initial value during the TPA. For Au supported on TiO_2(110) ($\langle d_0 \rangle$ = 3.88 nm and rsd = 25%), the corresponding T_{on} is 786 K.

To investigate the influence of composition, the ripening kinetics of the late TMs (Ag, Cu, Pd, Ni, Rh, Pt, Ru, and Ir) on TiO_2(110) were investigated during the TPA process. The initial PSD was assumed as Gaussian distribution with the average particle size $\langle d_0 \rangle$ = 3 nm and rsd = 10%. Evolution of the average diameter for late TMs considered with respect to the temperature is plotted in Figure 6a. Similar evolution behavior is seen for all TMs considered: the average diameter increases only when the ramping temperature reaches a threshold. The envelope shifts gradually toward higher temperature from Ag, Cu, Pd, Au, Ni, Rh, Pt, and Ru to Ir. Corresponding onset temperatures T_{on} are 472 K for Ag, 664 K for Cu, 752 K for Pd, 790 K for Au, 824 K for Ni, 1037 K for Rh, 1207 K for Pt, 1410 K for Ru, and 1623 K for Ir. It is striking that depending on the composition, T_{on} can vary by more than 1000 K. In Figure 6b, the calculated T_{on} is plotted with respect to E_{tot}, and a linear correlation between T_{on} and E_{tot} is established. The bigger the total activation energy, the higher the onset temperature. When E_{tot} increases from 1.41 eV (Ag) to 4.74 eV (Ir), corresponding T_{on} increases from 472 to 1623 K.

Although it remains difficult to extract the onset temperature experimentally in a consistent and systematical way, we tried to correlate the above calculations with relevant experiments. During annealing of Ag films deposited on TiO_2(110) from low temperature to 500 K for coverage of 1−2.4 ML, three-dimensional (3D) needlelike Ag islands were observed to occur on top of this Ag film. The ripening of small Ag clusters was proposed to dominate the formation process of these 3D islands.[88] The annealing temperature of 500 K necessary for this growth is close to the calculated T_{on} of 472 K for Ag particles on TiO_2(110). For the Pd particle growth on TiO_2(110),[47] the evolution of the size distribution observed in real time at high temperatures by STM was consistent with the OR mechanism. The operating temperatures of ripening at 750 K observed in the experiment is also close to the calculated T_{on} of 752 K. OR of large Au clusters on TiO_2(110) was directly observed by STM at elevated temperatures of about 750 K[42] and 800 K,[84] which are in agreement with the calculated T_{on} of 790 K as well. For Cu,[89] Ni,[90] Rh,[91] and Pt[45] on TiO_2(110), though their sintering mechanisms remain elusive, the observed sintering temperatures of 723, 880, 900, and 1303 K are also close to the calculated onset temperatures (664, 824, 1037, and 1207 K). Considering that the ripening kinetic is sensitive to several factors, including the average particle size, rsd,[51,53] defects,[17] preadsorbed species,[18] and so forth, the trend agreement between theory and experiment indicated in Figure 6b is satisfactory.

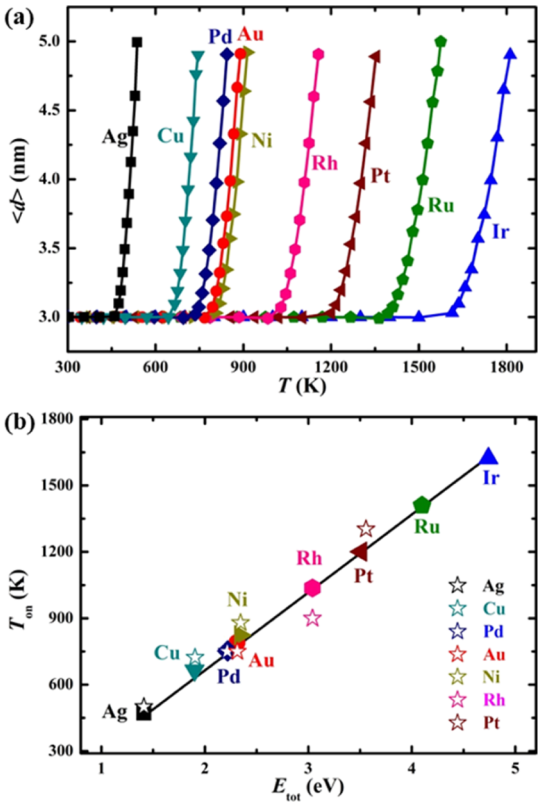

Figure 6. (a) Evolution of the average diameter of the late TM particles on TiO_2(110) with respect to the linear ramping of temperature from 200 K at a rate of 1 K/s and (b) corresponding onset temperature T_{on}. The contact angle α = 90°, initial $\langle d_0 \rangle$ = 3 nm, and rsd = 10%. The hollow stars corresponding to the metal by colors are reference to the experiment results: Ag,[88] Cu,[89] Pd,[47] Au,[42] Ni,[90] Rh,[91] and Pt.[45]

3.2.2. Isothermal Condition. Isothermal kinetic of Au/TiO_2(110) was also investigated to predict their long-time

DOI: 10.1021/acs.jpcc.8b08530
J. Phys. Chem. C 2019, 123, 1160−1169

durability against ripening. Here, the initial Gaussian PSD is set as $\langle d_0 \rangle$ = 3.5 nm and rsd = 10% estimated from reference (excluding the contribution from the TiO_x islands),[42] and ripening simulation is performed at 750 K. The resulted PSD (Figure 7a) is still LSW-like. Evolution of the average size $\langle d \rangle$,

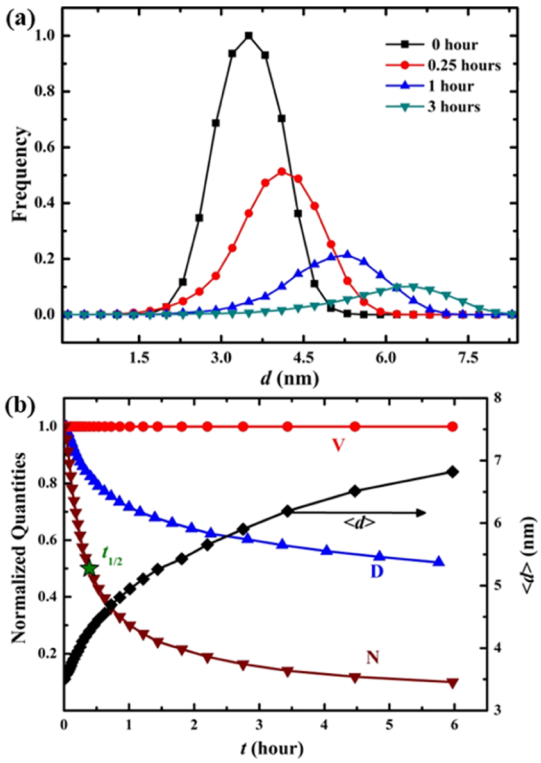

Figure 7. (a) Snapshots of PSD of Au particles on TiO_2(110) with time stream under isothermal condition of 750 K and (b) evolution of the normalized volume V (circle), dispersion D (triangle), particle number N (inverted triangle), and average diameter $\langle d \rangle$ with respect to the ripening time. Green star represents half-life time $t_{1/2}$. The contact angle α = 90°, initial $\langle d_0 \rangle$ = 3.5 nm, and rsd = 10%.

normalized dispersion D, and total particle number N are given in Figure 7b. As time increases, the calculated $\langle d \rangle$ increases, whereas the corresponding D and N decrease. Qualitatively, these are similar to the above kinetic results under TPA condition. However, there is one thing very different from TPA. Under isothermal condition, the rate of decay in dispersion and particle number becomes slow with the increase of time, whereas under TPA condition (Figure 5b), there is no obvious decrease in the ripening rate even at the very late stages. This is understandable since under TPA condition, the ramping temperature increases gradually with time, and the increase in the ramping temperature drives the ripening faster despite the fact that the average size increases as well.

From Figure 7b, it can be found that the calculated $\langle d \rangle$ increases from initial 3.5 nm to about 4 nm (0.25 h), 5 nm (1 h), and 6 nm (3 h) at 750 K. To compare with the experiment of TiO_2(110)-supported Au particles at 750 K,[42] we note that the contact angle was not available. By assuming the hemispherical shape with a contact angle of 90°, the particle diameter was found to increase from initial 3.5 to 2.6−4 nm (2 h) and 3.3−5.4 nm (36−42 h). Compared to the experiment, the calculated ripening rate is faster. The difference might come from the uncertainty mentioned above. Moreover, the influence of surface defects,[17,25,79] which is not considered in the present work, might enhance the metal−support interaction and slow down the ripening rate as well. Actually, by increasing E_{tot} from 2.31 to 2.52 eV, the resulting evolution of the average size agrees much better with the estimated experimental data.

To further study the influence of metal composition, we calculate the ripening kinetics for the late TMs considered with an initial PSD of $\langle d_0 \rangle$ = 3 nm and rsd = 10% at 500 K. Figure 8a shows the evolution of the average diameter with time on

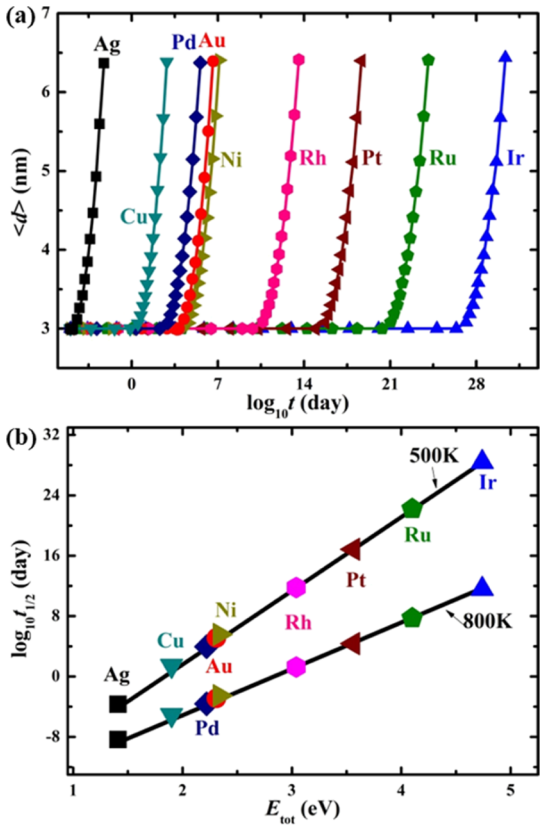

Figure 8. (a) Evolution of the average size for late TMs on TiO_2(110) with time in logarithm at 500 K. (b) Calculated half-life time $t_{1/2}$ varies with the total activation energy E_{tot} at 500 and 800 K. The contact angle α = 90°, initial $\langle d_0 \rangle$ = 3 nm, and rsd = 10%.

the logarithmic scale to span a rather large time scale. The half-life time $t_{1/2}$, corresponding to 50% reduction of N, is defined to facilitate the comparison. Calculated $t_{1/2}$ is plotted in Figure 8b with respect to E_{tot}. The higher the total activation energy, the longer the half-life time. Again, a perfect linear correlation (in logarithmic scale) between $t_{1/2}$ versus E_{tot} is found. Two aging temperatures of 500 and 800 K are considered. It can be found that with the increase of the aging temperature, the corresponding slope of the half-life time with respect to the total activation energy decreases, though the resulted difference between the metals considered remains considerably large.

3.3. Particle Size Effect. We address here the effect of the initial average size $\langle d_0 \rangle$ on ripening and how the initial size effect is modulated by the composition of the supported TMs. The calculated onset temperature T_{on} and half-life time $t_{1/2}$ for $\langle d_0 \rangle$ from 2 to 16 nm at a given rsd = 10% are plotted in Figure 9 for Pd/TiO_2(110). It can be found that with $\langle d_0 \rangle$ decreasing from 16 to 2 nm, T_{on} decreases from 1014 to 690 K, whereas

DOI: 10.1021/acs.jpcc.8b08530
J. Phys. Chem. C 2019, 123, 1160−1169

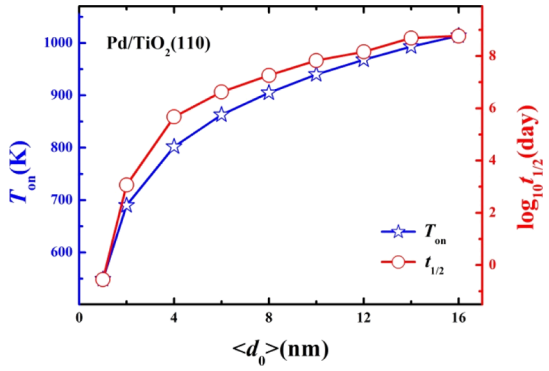

Figure 9. Calculated onset temperature T_{on} (under a linear ramping of temperature from 200 K at a rate of 1 K/s) and half-life time $t_{1/2}$ (at isothermal temperature of 500 K) as a function of the initial average diameter $\langle d_0 \rangle$ for Pd on TiO_2(110) and rsd = 10%.

$t_{1/2}$ decreases from $10^{8.8}$ to $10^{3.1}$ days. The huge size effect on the thermal stability and long-time durability, lowering T_{on} by about 324 K and $t_{1/2}$ by 5.7 orders of magnitude, is clearly seen. As dispersion increases only by about a factor of 8, the trade-off between stability and specific surface area should be seriously concerned.

We note that the influence of the initial average size on the ripening rate is not linear. For instance, when decreasing $\langle d_0 \rangle$ from 16 to 6 nm by 10 nm, T_{on} decreases by 151 K. However, on a further decrease from 6 to 2 nm by only 4 nm, T_{on} decreases by 173 K, which is even larger. Similarly, with $\langle d_0 \rangle$ decreasing from 16 to 6 nm, $t_{1/2}$ decreases by about 2 orders of magnitude, whereas further decreasing from 6 to 4 nm by only 2 nm, the decrease of $t_{1/2}$ is already as large as about 3.6 orders of magnitude. Namely, the smaller the initial average size, the higher the corresponding ripening rate. We note that though the supported particles with smaller initial average size grow faster, the resulting average size would not cross over those with a large initial average size. This is because the ripening rate will decrease rapidly with the growth of the average size. It is worthy to mention that these results are derived based on the assumption that the surface energy is constant with respect to the particle size. Actually, the surface energy is size-dependent and increases for the small particle.[49,59] This means that the thermal stability and half-life time of supported particles with a small initial average size are underestimated, and they would suffer more severe deactivation through ripening than the calculations indicated above.

Size effects on T_{on} and $t_{1/2}$ for all late TMs considered are plotted in Figure 10a,b, respectively. Irrespective of the late TM considered, both T_{on} and $t_{1/2}$ show consistent and similar dependence on the initial average size: the smaller the initial average size, the lower the thermal stability and the long-time durability. The calculated onset temperature and half-life time for Ag/TiO_2(110) are located at the bottom because it has the lowest total activation energy E_{tot} (Figures 6b and 8b). With a gradual increase of E_{tot}, the curves shift upward, and the calculated onset temperature and half-life time for Ir/TiO_2(110) with the highest E_{tot} are located at the top, as expected.

Depending on the metal composition, the size effect on the ripening is however different. For Ag/TiO_2(110), when decreasing $\langle d_0 \rangle$ from 16 to 2 nm, T_{on} and $t_{1/2}$ decrease by about 215 K and 5.1 orders of magnitude with the lowest E_{tot} of 1.41 eV, respectively. For Pd/TiO_2(110) with a larger E_{tot} of 2.22 eV, the extent of variation increases by 324 K and 5.7 orders of magnitude for the same decrease in $\langle d_0 \rangle$, whereas for Ir with the highest E_{tot} of 4.74 eV, the extent of variation increases further to 617 K and 6.8 orders of magnitude, which is larger than those of Pd. These results show that the extent of the size effect on stability increases with the total activation energy of ripening. For a given support, because the total activation energy of ripening is proportional to the corresponding cohesive energy of TMs (Figure 4), one can expect that the TMs with a high cohesive energy would have stronger size effect on the thermal stability and long-time durability.

For the platinum group metals considered, the calculated onset temperature could be as high as 1800 and 2100 K for Ru and Ir with a large initial average size. In reality, no catalyst support can survive at these temperatures. In turn, the mobility of the oxide support will cause it to sinter and encapsulate the metal particles long before reaching these temperatures. This actually results in the so-called strong metal−support interaction, which occurs typically on the platinum group metals (e.g., Pt, Ir, and Ru) with a high melting temperature.

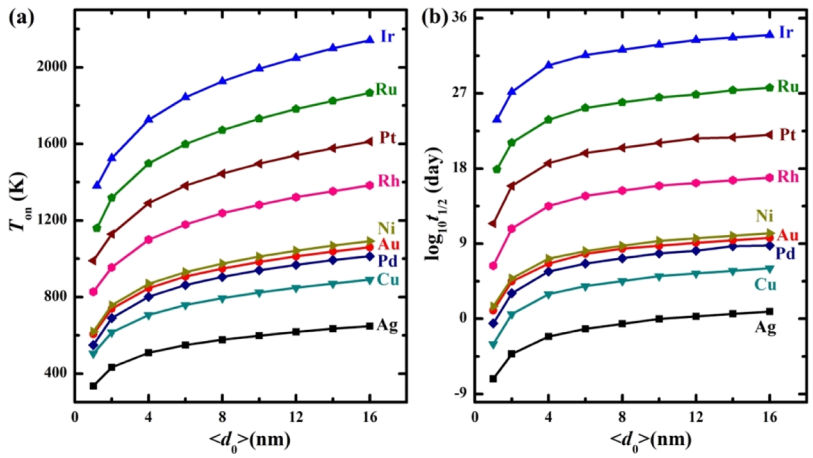

Figure 10. (a) Calculated onset temperature T_{on} as a function of the initial average diameter $\langle d_0 \rangle$ of late TM particles on TiO_2(110) under a linear ramping of temperature from 200 K at a rate of 1 K/s. (b) Calculated half-life time $t_{1/2}$ as a function of the initial average diameter $\langle d_0 \rangle$ at an isothermal temperature of 500 K. rsd = 10%.

DOI: 10.1021/acs.jpcc.8b08530
J. Phys. Chem. C 2019, 123, 1160−1169

Dependence of the thermal stability in terms of the onset temperature on the initial average particle size could be expressed empirically via the following formula

$$T_{on} = k_{on} T_m(B)\left(1 + \frac{\bar{d}}{\langle d_0 \rangle}\right)^{-1/q} \quad (5)$$

where $T_m(B)$ is the melting temperature of the bulk metal counterpart[81] and listed in Table 1. k_{on}, $\bar{d}$ and n are the fitting parameters. The fitted parameters and curves for different late TMs considered can be found in Table S3 and Figures S1−S9. Depending on the composition, k_{on}, $\bar{d}$ and q vary from 0.65 to 1.00, from 13 to 39 nm, and from 3.70 to 5.26. These parameters could relate to the metal−support interaction, characteristic length of ripening, and scaling behavior with respect to the particle size. To rationalize dependence of the onset temperature on the melting temperature of the bulk metal counterpart, we note that the latter is decided mainly by the corresponding cohesive energy.[92−94] As shown in Figure 4 for a given support, the total activation energy of the supported TM scales well with the cohesive energy of the bulk counterpart. On the other hand, the onset temperature depends linearly on the corresponding total activation energy (Figure 6b). As a result, the onset temperature of ripening scales well with the melting temperature of the corresponding bulk metal. In this context, Tamman temperature,[95] half of the bulk melting temperature, could also be used to estimate the onset of sintering. However, as indicated in the present work and our earlier works,[51,53,87] onset of sintering is sensitive to the PSD, metal−support interaction, and even the presence of reactants, which cannot be described simply by Tamman temperature alone.

4. CONCLUSIONS

We have used DFT to calculate the total activation energy of OR for late TM particles supported on TiO_2(110) surface. The total activation energy increases in the order of Ag < Cu < Pd < Au < Ni < Rh < Pt < Ru < Ir and varies from 1.41 to 4.74 eV. The difference in the total activation energy comes mainly from the formation energy, rather than the diffusion barrier, of the metal monomer on supports. Ostwald ripening under temperature program aging and isothermal condition was explored for TiO_2(110)-supported late TM particles. It is found that the composition of supported TMs has enormous impact on their thermal stability and long-time durability against ripening. From Ag to Ir, the corresponding half-life time increases exponentially with the total activation energy, whereas the onset temperature of ripening varies more than hundreds of kelvin in good agreement with the available experiment. The initial average particle size significantly impacts thermal stability and long-time durability, and the corresponding size effect further increases for metals with higher total activation energy.

ASSOCIATED CONTENT

Supporting Information

The Supporting Information is available free of charge on the ACS Publications website at DOI: 10.1021/acs.jpcc.8b08530.

Calculated diffusion barrier, formation energy by PBE and RPBE, and fitting curves (PDF)

AUTHOR INFORMATION

Corresponding Authors

*E-mail: cqchen@hust.edu.cn (C.C.).
*E-mail: wxli70@ustc.edu.cn (W.-X.L.).

ORCID

Wei-Xue Li: 0000-0002-5043-3088

Author Contributions

⊥Q.W. and S.H. contributed equally.

Notes

The authors declare no competing financial interest.

ACKNOWLEDGMENTS

We acknowledge funding from the National Key R&D Program of China (2018YFA0208603 and 2017YFB0602200), the Natural Science Foundation of China (91645202), and the Chinese Academy of Sciences (QYZDJ-SSW-SLH054).

REFERENCES

(1) Fu, Q.; Wagner, T. Interaction of nanostructured metal overlayers with oxide surfaces. *Surf. Sci. Rep.* **2007**, *62*, 431−498.
(2) Maeda, Y.; Akita, T.; Okumura, M.; Kohyama, M. Local Barrier Height of Ir/TiO_2 Model Catalysts. *Jpn. J. Appl. Phys.* **2004**, *43*, 4595−4598.
(3) Dehghani, N.; Yousefiazari, E. A gas sensor comprising two back-to-back connected Au/TiO_2 Schottky diodes. *Mater. Res. Express* **2018**, *5*, 046304.
(4) Zhang, M.; Yuan, Z.; Song, J.; Zheng, C. Improvement and mechanism for the fast response of a Pt/TiO_2 gas sensor. *Sens. Actuators, B* **2010**, *148*, 87−92.
(5) Yang, F.; Deng, D.; Pan, X.; Fu, Q.; Bao, X. Understanding nano effects in catalysis. *Natl. Sci. Rev.* **2015**, *2*, 183−201.
(6) Bartholomew, C. H. Mechanisms of catalyst deactivation. *Appl. Catal., A* **2001**, *212*, 17−60.
(7) Forzatti, P.; Lietti, L. Catalyst deactivation. *Catal. Today* **1999**, *52*, 165−181.
(8) McCarty, J. G.; Gusman, M.; Lowe, D. M.; Hildenbrand, D. L.; Lau, K. N. Stability of supported metal and supported metal oxide combustion catalysts. *Catal. Today* **1999**, *47*, 5−17.
(9) Houk, L. R.; Challa, S. R.; Grayson, B.; Fanson, P.; Datye, A. K. The Definition of "Critical Radius" for a Collection of Nanoparticles Undergoing Ostwald Ripening. *Langmuir* **2009**, *25*, 11225−11227.
(10) Prévot, G. Ostwald ripening of three-dimensional clusters on a surface studied with an ultrafast kinetic Monte Carlo algorithm. *Phys. Rev. B: Condens. Matter Mater. Phys.* **2011**, *84*, 045434.
(11) Simonsen, S. B.; Chorkendorff, I.; Dahl, S.; Skoglundh, M.; Sehested, J.; Helveg, S. Ostwald ripening in a Pt/SiO_2 model catalyst studied by in situ TEM. *J. Catal.* **2011**, *281*, 147−155.
(12) Kandel, D. Selection of the scaling solution in a cluster coalescence model. *Phys. Rev. Lett.* **1997**, *79*, 4238−4241.
(13) Palasantzas, G.; Vystavel, T.; Koch, S. A.; De Hosson, J. T. M. Coalescence aspects of cobalt nanoparticles duringin situhigh-temperature annealing. *J. Appl. Phys.* **2006**, *99*, 024307.
(14) Ruckenstein, E.; Pulvermacher, B. Growth kinetics and the size distributions of supported metal crystallites. *J. Catal.* **1973**, *29*, 224−245.
(15) Hansen, T. W.; DeLaRiva, A. T.; Challa, S. R.; Datye, A. K. Sintering of catalytic nanoparticles: particle migration or ostwald ripening? *Acc. Chem. Res.* **2013**, *46*, 1720−1730.
(16) Bowker, M.; Fourré, E. Direct interactions between metal nanoparticles and support: STM studies of Pd on TiO_2(110). *Appl. Surf. Sci.* **2008**, *254*, 4225−4229.
(17) Tabib Zadeh Adibi, P.; Pingel, T.; Olsson, E.; Grönbeck, H.; Langhammer, C. Pt nanoparticle sintering and redispersion on a heterogeneous nanostructured support. *J. Phys. Chem. C* **2016**, *120*, 14918−14925.

DOI: 10.1021/acs.jpcc.8b08530
J. Phys. Chem. C 2019, 123, 1160−1169

(18) Addou, R.; Senftle, T. P.; O'Connor, N.; Janik, M. J.; van Duin, A. C. T.; Batzill, M. Influence of Hydroxyls on Pd Atom Mobility and Clustering on Rutile TiO2(011)-2 × 1. *ACS Nano* **2014**, *8*, 6321−6333.
(19) Lu, J.-L.; Gao, H.-J.; Shaikhutdinov, S.; Freund, H.-J. Gold supported on well-ordered ceria films: nucleation, growth and morphology in CO oxidation reaction. *Catal. Lett.* **2007**, *114*, 8−16.
(20) Evans, J.; Hayden, B.; Mosselmans, F.; Murray, A. The chemistry of rhodium on TiO_2(110) deposited by MOCVD oc$(CO)_2Cl]_2$ and MVD. *Surf. Sci.* **1994**, *301*, 61−82.
(21) Simonsen, S. B.; Chorkendorff, I.; Dahl, S.; Skoglundh, M.; Meinander, K.; Jensen, T. N.; Lauritsen, J. V.; Helveg, S. Effect of particle morphology on the ripening of supported pt nanoparticles. *J. Phys. Chem. C* **2012**, *116*, 5646−5653.
(22) Wettergren, K.; Schweinberger, F. F.; Deiana, D.; Ridge, C. J.; Crampton, A. S.; Rötzer, M. D.; Hansen, T. W.; Zhdanov, V. P.; Heiz, U.; Langhammer, C. High sintering resistance of size-selected platinum cluster catalysts by suppressed ostwald ripening. *Nano Lett.* **2014**, *14*, 5803−5809.
(23) Su, Y.-Q.; Liu, J.-X.; Filot, I. A. W.; Hensen, E. J. M. Theoretical study of ripening mechanisms of pd clusters on ceria. *Chem. Mater.* **2017**, *29*, 9456−9462.
(24) Popescu, R.; Schneider, R.; Gerthsen, D.; Böttcher, A.; Löffler, D.; Weis, P.; Kappes, M. M. Coarsening of mass-selected Au clusters on amorphous carbon at room temperature. *Surf. Sci.* **2009**, *603*, 3119−3125.
(25) Iachella, M.; Le Bahers, T.; Loffreda, D. Diffusion Kinetics of Gold and Copper Atoms on Pristine and Reduced Rutile TiO_2 (110) Surfaces. *J. Phys. Chem. C* **2018**, *122*, 3824−3837.
(26) Aizawa, M.; Lee, S.; Anderson, S. L. Sintering, oxidation, and chemical properties of size-selected nickel clusters on TiO_2(110). *J. Chem. Phys.* **2002**, *117*, 5001−5011.
(27) Zhou, J.; Kang, Y. C.; Ma, S.; Chen, D. A. Adsorbate-induced dissociation of metal clusters: TiO_2(110)-supported Cu and Ni clusters exposed to oxygen gas. *Surf. Sci.* **2004**, *562*, 113−127.
(28) Anastasopoulos, A.; Hayden, B. E. TiO_2(110)-(1×1) supported Cu particles: An FT-RAIRS investigation. *Surf. Sci.* **2011**, *605*, 174−178.
(29) Diebold, U.; Pan, J.-M.; Madey, T. E. Growth mode of ultrathin copper overlayers on TiO_2(110). *Phys. Rev. B: Condens. Matter Mater. Phys.* **1993**, *47*, 3868−3876.
(30) Omotoso, T.; Boonyasuwat, S.; Crossley, S. P. Understanding the role of TiO_2 crystal structure on the enhanced activity and stability of Ru/TiO_2 catalysts for the conversion of lignin-derived oxygenates. *Green Chem.* **2014**, *16*, 645−652.
(31) Stone, P.; Smith, R. D.; Bowker, M. The structure and reactivity of anchored nanoparticles on a reducible support. *Faraday Discuss.* **2004**, *125*, 379−390.
(32) Khosravian, H. Synthesis and characterization of rhodium nanoclusters on TiO_2 (110) surface using organometallic compounds. *Surf. Sci.* **2018**, *667*, 38−44.
(33) Bugyi, L.; Óvári, L.; Kónya, Z. The formation and stability of Rh nanostructures on TiO_2(110) surface and TiO_x encapsulation layers. *Appl. Surf. Sci.* **2013**, *280*, 60−66.
(34) Fu, Q.; Wagner, T.; Olliges, S.; Carstanjen, H.-D. Metal−Oxide Interfacial Reactions: Encapsulation of Pd on TiO_2(110). *J. Phys. Chem. B* **2005**, *109*, 944−951.
(35) Suzuki, T.; Souda, R. The encapsulation of Pd by the supporting TiO_2(110) surface induced by strong metal-support interactions. *Surf. Sci.* **2000**, *448*, 33−39.
(36) Lai, X.; St. Clair, T. P.; Wayne Goodman, D. Oxygen-induced morphological changes of Ag nanoclusters supported on TiO_2(110). *Faraday Discuss.* **1999**, *114*, 279−284.
(37) Sun, J.; Ma, D.; Zhang, H.; Liu, X.; Han, X.; Bao, X.; Weinberg, G.; Pfänder, N.; Su, D. Toward monodispersed silver nanoparticles with unusual thermal stability. *J. Am. Chem. Soc.* **2006**, *128*, 15756−15764.
(38) Berkó, A.; Solymosi, F. Effects of Different Gases on the Morphology of Ir Nanoparticles Supported on the TiO_2(110)-(1×2) Surface. *J. Phys. Chem. B* **2000**, *104*, 10215−10221.
(39) Aizawa, M.; Lee, S.; Anderson, S. L. Deposition dynamics and chemical properties of size-selected Ir clusters on TiO_2. *Surf. Sci.* **2003**, *542*, 253−275.
(40) Berkó, A.; Szökő, J.; Solymosi, F. Effect of CO on the morphology of Pt nanoparticles supported on TiO_2(110)-(1×n). *Surf. Sci.* **2004**, *566-568*, 337−342.
(41) Sánchez-Sánchez, C.; Martín-Gago, J. A.; López, M. F. Small Pt nanoparticles on the TiO_2(110)-(1×2) surface. *Surf. Sci.* **2013**, *607*, 159−163.
(42) Mitchell, C. E. J.; Howard, A.; Carney, M.; Egdell, R. G. Direct observation of behaviour of Au nanoclusters on TiO_2(110) at elevated temperatures. *Surf. Sci.* **2001**, *490*, 196−210.
(43) Gao, W.; Sivaramakrishnan, S.; Wen, J.; Zuo, J.-M. Direct Observation of Interfacial Au Atoms on TiO_2 in Three Dimensions. *Nano Lett.* **2015**, *15*, 2548−2554.
(44) Yang, F.; Chen, M. S.; Goodman, D. W. Sintering of Au Particles Supported on TiO_2(110) during CO Oxidation. *J. Phys. Chem. C* **2008**, *113*, 254−260.
(45) Behafarid, F.; Roldan Cuenya, B. Coarsening phenomena of metal nanoparticles and the influence of the support pre-treatment: Pt/TiO_2(110). *Surf. Sci.* **2012**, *606*, 908−918.
(46) Jak, M. J. J.; Konstapel, C.; van Kreuningen, A.; Verhoeven, J.; Frenken, J. W. M. Scanning tunnelling microscopy study of the growth of small palladium particles on TiO_2(110). *Surf. Sci.* **2000**, *457*, 295−310.
(47) Howard, A.; Mitchell, C. E. J.; Egdell, R. G. Real time STM observation of Ostwald ripening of Pd nanoparticles on TiO_2(110) at elevated temperature. *Surf. Sci.* **2002**, *515*, L504−L508.
(48) Wynblatt, P.; Gjostein, N. A. Supported metal crystallites. *Prog. Solid State Chem.* **1975**, *9*, 21−58.
(49) Parker, S. C.; Campbell, C. T. Kinetic model for sintering of supported metal particles with improved size-dependent energetics and applications to Au on TiO_2(110). *Phys. Rev. B: Condens. Matter Mater. Phys.* **2007**, *75*, 035430.
(50) Kang, S. B.; Lim, J. B.; Jo, D.; Nam, I.-S.; Cho, B. K.; Hong, S. B.; Kim, C. H.; Oh, S. H. Ostwald-ripening sintering kinetics of Pd-based three-way catalyst: Importance of initial particle size of Pd. *Chem. Eng. J.* **2017**, *316*, 631−644.
(51) Hu, S.; Li, W.-X. Influence of particle size distribution on lifetime and thermal stability of ostwald ripening of supported particles. *ChemCatChem* **2018**, *10*, 2900−2907.
(52) Goldsmith, B. R.; Sanderson, E. D.; Ouyang, R.; Li, W.-X. CO- and NO-induced disintegration and redispersion of three-way catalysts rhodium, palladium, and platinum: an ab initio thermodynamics study. *J. Phys. Chem. C* **2014**, *118*, 9588−9597.
(53) Hu, S.; Li, W.-X. Theoretical investigation of metal-support interactions on ripening kinetics of supported particles. *ChemNanoMat* **2018**, *4*, 510−517.
(54) Ouyang, R.; Liu, J.-X.; Li, W.-X. Atomistic theory of ostwald ripening and disintegration of supported metal particles under reaction conditions. *J. Am. Chem. Soc.* **2013**, *135*, 1760−1771.
(55) Carrillo, J.-M. Y.; Raphael, E.; Dobrynin, A. V. Adhesion of nanoparticles. *Langmuir* **2010**, *26*, 12973−12979.
(56) Li, H.-T.; Chen, L.-F.; Yuan, X.; Zhang, W.-Q.; Smith, J. R.; Evans, A. G. Interfacial stoichiometry and adhesion at metal/α-Al_2O_3 interfaces. *J. Am. Ceram. Soc.* **2011**, *94*, s154−s159.
(57) Johnson, C. A. Generalization of the Gibbs-Thomson equation. *Surf. Sci.* **1965**, *3*, 429−444.
(58) Tran, R.; Xu, Z.; Radhakrishnan, B.; Winston, D.; Sun, W.; Persson, K. A.; Ong, S. P. Surface energies of elemental crystals. *Sci. Data* **2016**, *3*, 160080.
(59) Medasani, B.; Park, Y. H.; Vasiliev, I. Theoretical study of the surface energy, stress, and lattice contraction of silver nanoparticles. *Phys. Rev. B: Condens. Matter Mater. Phys.* **2007**, *75*, 235436.

DOI: 10.1021/acs.jpcc.8b08530
J. Phys. Chem. C 2019, 123, 1160−1169

(60) Farmer, J. A.; Campbell, C. T. Ceria maintains smaller metal catalyst particles by strong metal-support bonding. *Science* **2010**, *329*, 933−936.
(61) Hemmingson, S. L.; Campbell, C. T. Trends in adhesion energies of metal nanoparticles on oxide surfaces: understanding support effects in catalysis and nanotechnology. *ACS Nano* **2017**, *11*, 1196−1203.
(62) Parker, S. C.; Campbell, C. T. Reactivity and sintering kinetics of Au/TiO_2(110) model catalysts: particle size effects. *Top. Catal.* **2007**, *44*, 3−13.
(63) Barnard, A. S.; Zapol, P.; Curtiss, L. A. Anatase and rutile surfaces with adsorbates representative of acidic and basic conditions. *Surf. Sci.* **2005**, *582*, 173−188.
(64) Overbury, S. H.; Bertrand, P. A.; Somorjai, G. A. Surface composition of binary systems. Prediction of surface phase diagrams of solid solutions. *Chem. Rev.* **1975**, *75*, 547−560.
(65) Tyson, W. R.; Miller, W. A. Surface free energies of solid metals: Estimation from liquid surface tension measurements. *Surf. Sci.* **1977**, *62*, 267−276.
(66) Kresse, G.; Furthmüller, J. Efficient iterative schemes for ab initio total-energy calculations using a plane-wave basis set. *Phys. Rev. B: Condens. Matter Mater. Phys.* **1996**, *54*, 11169−11186.
(67) Kresse, G.; Furthmüller, J. Efficiency of ab-initio total energy calculations for metals and semiconductors using a plane-wave basis set. *Comput. Mater. Sci.* **1996**, *6*, 15−50.
(68) Kresse, G.; Hafner, J. Ab initio molecular dynamics for liquid metals. *Phys. Rev. B: Condens. Matter Mater. Phys.* **1993**, *47*, 558−561.
(69) Hammer, B.; Hansen, L. B.; Nørskov, J. K. Improved adsorption energetics within density-functional theory using revised Perdew-Burke-Ernzerhof functionals. *Phys. Rev. B: Condens. Matter Mater. Phys.* **1999**, *59*, 7413−7421.
(70) Grant, F. A. Properties of rutile (titanium dioxide). *Rev. Mod. Phys.* **1959**, *31*, 646−674.
(71) Kim, H. Y.; Lee, H. M.; Pala, R. G. S.; Shapovalov, V.; Metiu, H. CO Oxidation by Rutile TiO_2(110) Doped with V, W, Cr, Mo, and Mn. *J. Phys. Chem. C* **2008**, *112*, 12398−12408.
(72) Feynman, R. P. Forces in molecules. *Phys. Rev.* **1939**, *56*, 340−343.
(73) Henkelman, G.; Jónsson, H. Improved tangent estimate in the nudged elastic band method for finding minimum energy paths and saddle points. *J. Chem. Phys.* **2000**, *113*, 9978−9985.
(74) Henkelman, G.; Uberuaga, B. P.; Jónsson, H. A climbing image nudged elastic band method for finding saddle points and minimum energy paths. *J. Chem. Phys.* **2000**, *113*, 9901−9904.
(75) Cai, Y.; Bai, Z.; Chintalapati, S.; Zeng, Q.; Feng, Y. P. Transition metal atoms pathways on rutile TiO_2 (110) surface: Distribution of Ti^{3+} states and evidence of enhanced peripheral charge accumulation. *J. Chem. Phys.* **2013**, *138*, 154711.
(76) Zhao, W.; Lin, H.; Li, Y.; Zhang, Y.; Huang, X.; Chen, W. Growth mechanism of palladium clusters on rutile TiO_2(110) surface. *J. Nat. Gas Chem.* **2012**, *21*, 544−555.
(77) Sanz, J. F.; Márquez, A. Adsorption of Pd Atoms and Dimers on the TiO_2(110) Surface: A First Principles Study. *J. Phys. Chem. C* **2007**, *111*, 3949−3955.
(78) Chang, T.-Y.; Tanaka, Y.; Ishikawa, R.; Toyoura, K.; Matsunaga, K.; Ikuhara, Y.; Shibata, N. Direct Imaging of Pt Single Atoms Adsorbed on TiO_2(110) Surfaces. *Nano Lett.* **2013**, *14*, 134−138.
(79) Iddir, H.; Öğüt, S.; Browning, N. D.; Disko, M. M. Adsorption and diffusion of Pt and Au on the stoichiometric and reduced TiO_2 rutile (110) surfaces. *Phys. Rev. B: Condens. Matter Mater. Phys.* **2005**, *72*, No. 081407(R).
(80) Mutombo, P.; Balázs, N.; Majzik, Z.; Berkó, A.; Cháb, V. Theoretical study of the adsorption of rhodium on a TiO_2(110)-1×1 surface. *Appl. Surf. Sci.* **2012**, *258*, 4478−4482.
(81) Kittel, C. *Introduction to Solid State*; John Wiley & Sons, 1966.
(82) Park, J. B.; Ratliff, J. S.; Ma, S.; Chen, D. A. In situ scanning tunneling microscopy studies of bimetallic cluster growth: Pt-Rh on TiO_2(110). *Surf. Sci.* **2006**, *600*, 2913−2923.
(83) Zhou, J.; Kang, Y. C.; Chen, D. A. Controlling island size distributions: a comparison of nickel and copper growth on TiO_2. *Surf. Sci.* **2003**, *537*, L429−L434.
(84) Maeda, Y.; Fujitani, T.; Tsubota, S.; Haruta, M. Size and density of Au particles deposited on TiO_2(110)-(1×1) and cross-linked (1×2) surfaces. *Surf. Sci.* **2004**, *562*, 1−6.
(85) Akita, T.; Lu, P.; Ichikawa, S.; Tanaka, K.; Haruta, M. Analytical TEM study on the dispersion of Au nanoparticles in Au/TiO_2 catalyst prepared under various temperatures. *Surf. Interface Anal.* **2001**, *31*, 73−78.
(86) Lai, X.; Goodman, D. W. Structure-reactivity correlations for oxide-supported metal catalysts: new perspectives from STM. *J. Mol. Catal. A: Chem.* **2000**, *162*, 33−50.
(87) Hu, S.; Ouyang, R.; Li, W.-X. First-principles kinetics study of carbon monoxide promoted Ostwald ripening of Au particles on FeO/Pt(111). *J. Energy Chem.* **2018**, DOI: 10.1016/j.jechem.2018.03.023.
(88) Su, C.; Yeh, J.-C.; Lin, J.-L.; Lin, J.-C. The growth of Ag films on a TiO_2(110)-(1×1) surface. *Appl. Surf. Sci.* **2001**, *169-170*, 366−370.
(89) Carroll, D. L.; Wagner, M.; Rühle, M.; Bonnell, D. A. The Thermal Stability of Thin Copper Films Deposited on TiO_2(110) Studied by Scanning Tunneling Microscopy. *J. Mater. Res.* **2011**, *12*, 975−983.
(90) Tanner, R. E.; Goldfarb, I.; Castell, M. R.; Briggs, G. A. D. The evolution of Ni nanoislands on the rutile TiO_2(110) surface with coverage, heating and oxygen treatment. *Surf. Sci.* **2001**, *486*, 167−184.
(91) Berkó, A.; Ménesi, G.; Solymosi, F. STM study of rhodium deposition on the TiO_2(110)-(1 × 2) surface. *Surf. Sci.* **1997**, *372*, 202−210.
(92) Nanda, K. K.; Sahu, S. N.; Behera, S. N. Liquid-drop model for the size-dependent melting of low-dimensional systems. *Phys. Rev. A* **2002**, *66*, 013208.
(93) Tateno, J. An empirical relation on the melting temperature of some ionic crystals. *Solid State Commun.* **1972**, *10*, 61−62.
(94) Sun, C. Q. Oxidation electronics: bond-band-barrier correlation and its applications. *Prog. Mater. Sci.* **2003**, *48*, 521−685.
(95) Moulijn, J. A.; van Diepen, A. E.; Kapteijn, F. Catalyst deactivation: is it predictable?What to do? *Appl. Catal., A* **2001**, *212*, 3−16.

DOI: 10.1021/acs.jpcc.8b08530
J. Phys. Chem. C 2019, 123, 1160−1169